



HHS Public Access

Author manuscript

Nature. Author manuscript; available in PMC 2013 May 22.

Published in final edited form as:

Nature. 2012 November 22; 491(7425): 599–602. doi:10.1038/nature11554.

Synaptic amplification by dendritic spines enhances input cooperativity

Mark T. Harnett^{1,*}, Judit K. Makara^{1,2,*}, Nelson Spruston¹, William L. Kath³, and Jeffrey C. Magee^{1,‡}

¹HHMI Janelia Farm Research Campus, Ashburn, VA 20147 USA

²Institute of Experimental Medicine, Hungarian Academy of Sciences, Budapest 1083, Hungary

³Departments of Applied Mathematics and Neurobiology, Northwestern University, Evanston, IL, 60208 USA

Abstract

Dendritic spines are the nearly ubiquitous site of excitatory synaptic input onto neurons^{1–2} and as such are critically positioned to influence diverse aspects of neuronal signaling. Decades of theoretical studies have proposed that spines may function as highly effective and modifiable chemical and electrical compartments that regulate synaptic efficacy, integration, and plasticity^{3–8}. Experimental studies have confirmed activity-dependent structural dynamics and biochemical compartmentalization by spines^{9–12}. However, a longstanding debate remains over the influence of spines on the electrical aspects of synaptic transmission and dendritic operation^{3–8,13–18}. Here, we measured the amplitude ratio (AR) of spine head to parent dendrite voltage across a range of dendritic compartments and calculated the associated R_{neck} for spines at apical trunk dendrites in hippocampal CA1 pyramidal neurons. We found that R_{neck} is large enough ($\sim 500 \text{ M}\Omega$) to substantially amplify the spine head depolarization associated with a unitary synaptic input by ~ 1.5 - to ~ 45 -fold depending on parent dendritic impedance. A morphologically realistic compartmental model capable of reproducing the observed spatial profile of AR indicates that spines provide a consistently high impedance input structure throughout the dendritic arbor. Finally, we demonstrate that the amplification produced by spines encourages electrical interaction among coactive inputs through an R_{neck} -dependent increase in spine head voltage-dependent conductance activation. We conclude that the electrical properties of spines promote nonlinear dendritic processing and associated forms of plasticity and storage, thus fundamentally enhancing the computational capabilities of neurons^{19–21}.

Users may view, print, copy, download and text and data- mine the content in such documents, for the purposes of academic research, subject always to the full Conditions of use: http://www.nature.com/authors/editorial_policies/license.html#terms

[‡]Correspondence to: Jeffrey C. Magee, Howard Hughes Medical Institute, Janelia Farm Research Campus, 19700 Helix Dr, Ashburn, VA 20147, USA, mageej@janelia.hhmi.org.

^{*}These authors contributed equally to this work and are listed in alphabetical order.

Supplementary Information is linked to the online version of the paper at www.nature.com/nature.

Author Contributions M.H., J.K.M. and J.C.M. conceived the project and designed the experiments. M.H. and J.K.M performed all experiments and data analysis. N.S., W.K., and J.C.M performed computer simulations. M.H., J.K.M. and J.C.M. wrote the paper with comments from all authors.

Reprints and permissions information is available at www.nature.com/reprints.

The authors declare no competing financial interests.

To measure the ratio of spine-to-dendrite voltage amplitude and associated spine neck resistance (R_{neck}), we combined two-photon Ca^{2+} imaging and glutamate uncaging with dual dendritic patch-clamp current injection and voltage recording from hippocampal CA1 pyramidal neurons in acute slices from adult rats. Excitatory input was produced by uncaging onto a single spine of interest located on the apical dendritic trunk. The resulting EPSP was measured in the dendritic branch (termed $\text{EPSP}_{\text{branch}}$; see Methods) and laser power was modulated to generate a range of $\text{EPSP}_{\text{branch}}$ amplitudes and associated spine head Ca^{2+} signals (assayed via OGB-1) that were mediated exclusively by voltage-gated Ca^{2+} channels (VGCC; Fig. 1b, e, f; 0.5–1 μM TTX and 50–100 μM D-AP5 present; Supplementary Figs. 2–4). Next, excitatory postsynaptic current (EPSC)-shaped currents were injected into the dendrite to depolarize the spine to a level where the associated spine Ca^{2+} signals matched those produced by the glutamate uncaging (Fig. 1c–f & Supplementary Figure 9; $8.6 \pm 1.0 \mu\text{m}$ between pipettes, $14.2 \pm 1.7 \mu\text{m}$ from spine of interest to voltage recording electrode). Due to the lack of voltage attenuation from the dendrite to the spine^{3,4,6}, these dendritic depolarizations provide an accurate estimate of the amplitude of spine head potentials (termed $\text{EPSP}_{\text{spine}}$; see Methods). The amount of electrical compartmentalization produced by the spine was measured as the amplitude ratio (AR) of $\text{EPSP}_{\text{spine}}$ to $\text{EPSP}_{\text{branch}}$. R_{neck} was subsequently calculated from this value and the measured dendritic impedance ($R_{\text{d-epsc}}$; $11.0 \pm 1.0 \text{ M}\Omega$, $n = 8$ cells, Equation 4 in Methods). For apical trunk spines located $223 \pm 10 \mu\text{m}$ from the soma we measured an AR of 49.0 ± 3.8 and corresponding R_{neck} of $514 \pm 44 \text{ M}\Omega$ ($n = 10$ spines from 8 cells, Fig. 1g). A morphologically realistic multi-compartmental simulation using an R_{neck} of 500 $\text{M}\Omega$ for trunk spines at similar locations supported the above observations (Fig. 1i, j). Under physiological conditions, the mean unitary dendritic EPSP amplitude at these synapses is $\sim 0.5 \text{ mV}^{22}$. Together with our measurements above, this reported value suggests spine head depolarizations of $\sim 25 \text{ mV}$ for an average unitary event. These data indicate that spines function as high-impedance input compartments that passively amplify synaptic depolarization locally within the spine head to well over what could be achieved by synapses directly onto dendrites. Thus, unitary synaptic inputs may significantly recruit active spine voltage-dependent conductances^{5,8,14,17,23} such as NMDA receptors (Supplementary Fig. 1; see also Fig. 4).

We next compared the electrical properties of spines across various dendritic compartments. Due to the inaccessibility of small diameter oblique branches, we replaced dendritic current injection with multi-site glutamate uncaging techniques to estimate $\text{EPSP}_{\text{spine}}$ (see Methods; Fig. 2 and Supplementary Figs. 2–4,6,8). We observed that spine-to-branch AR was much lower in apical oblique dendrites than in the trunk and continued to decline significantly from originating branch points to more distal sites (Fig. 2a–e, AR: 7.8 ± 0.5 , $n = 7$ spines from 7 cells for proximal sites, 3.6 ± 0.3 , $n = 10$ spines from 7 cells for medial sites, and 1.7 ± 0.1 , $n = 9$ spines from 6 cells for distal sites, $p < 0.0001$, one-way ANOVA). Similar ratios were found at the terminal ends of oblique dendrites (within $8 \mu\text{m}$ of the end) for EPSPs evoked with a rapid stimulation paradigm (see Methods; Fig. 2e, red symbols, AR: 1.7 ± 0.2 , $n = 12$ spines from 8 cells). Consistent with this small ratio, input onto a single spine triggered significant Ca^{2+} signals in other nearby spines at these distal locations (Supplementary Fig. 5a–d). These data indicate that the level of passive synaptic

amplification produced by R_{neck} is dependent on dendritic properties with the greatest effect at the largest compartments.

A morphologically realistic computer model was used to examine the factors involved in producing the above spatial patterns of $\text{EPSP}_{\text{branch}}$, $\text{EPSP}_{\text{spine}}$ and AR. A simple model where the dendritic location of the input was varied while R_{neck} was held constant at 500 $\text{M}\Omega$ completely reproduced all experimental observations (Fig. 3a–c). These results indicate that the spatial profile of passive spine amplification (~30 fold decrease from trunk to branch end) reported in Fig. 2 could result solely from expected changes in local dendritic impedance^{3,4,6}. When the converse simulation was implemented (*i.e.* local dendritic impedance was held constant and R_{neck} was reduced with distance), additional implausible and experimentally unsupported manipulations were required (see Computational Methods). This strongly suggests that R_{neck} does not systematically change across different dendritic compartments (see Supplementary Fig. 6 for intra-regional variation in R_{neck}) and that the level of depolarization within the spine head is relatively independent of the local impedance profile of the dendrite (see Supplementary Cable Theory). However, the size of synaptic depolarization in the parent dendrite will vary dramatically (increasing ~30 fold from trunk to branch end) due to proportional changes in the impedance of different dendritic compartments. This effect could produce the relative location independence of $\text{EPSP}_{\text{branch}}$ observed in Fig. 2f & g²⁴. Altogether, the presence of a large, yet modifiable, R_{neck} allows dendritic spines to function as consistent, yet adjustable, high impedance input structures throughout the apical dendritic arborization of CA1 pyramidal neurons^{14,15,25}.

Of the parameters affecting dendritic impedance (axial resistance, r_a ; membrane capacitance, c_m ; membrane resistance, r_m) only r_m is readily modulated. We therefore investigated the role of r_m in spine electrical function by blocking a variety of voltage-dependent ion channels (Fig. 3d–h). Bath application of BaCl_2 (250–400 μM) and ZD7288 (10 μM) increased steady-state dendritic membrane resistance ($R_{\text{d-ss}}$; measured 262 \pm 33 μm from the soma) from 31.6 \pm 3.2 $\text{M}\Omega$ to 133.2 \pm 7.7 $\text{M}\Omega$ ($p < 0.0001$, paired t-test, $n = 6$). As expected from theoretical considerations (see Supplementary Cable Theory), this large increase in r_m did not significantly alter AR (23.2 \pm 1.7 vs. 21.1 \pm 1.5, $n = 6$ spines from 6 cells, $p = 0.097$, paired t-test, for trunk spines 285 \pm 36 μm from soma). Additionally, altering resting conductance over several orders of magnitude had essentially no impact on AR in the model (see Supplementary Cable Theory)²⁴. These results illustrate that, in addition to R_{neck} , the most important determinants of passive spine voltage amplification are morphological factors that control the magnitude of axial current (*i.e.* dendritic diameter as well as proximity to branch and end points). Because such factors are not easily modified, changes in spine neck resistance would be the most tenable approach to altering the amplifying properties of spines^{14,15}.

The passive amplification capabilities of spines could potentially increase the recruitment of active voltage-dependent conductances at the site of input^{5,8,14,17,23}, thereby enhancing interactions among multiple synaptic inputs. To test this idea we employed multi-site uncaging and simultaneous Ca^{2+} imaging with NMDARs intact to produce voltage and single spine Ca^{2+} input-output curves at individual apical oblique branches (Fig. 4a–c). Single inputs evoked small but significant Ca^{2+} influx (~25% $\Delta\text{F}/\text{F}$) into activated spines

and recruitment of additional inputs increased spine Ca^{2+} signals and membrane depolarization in an NMDAR-dependent nonlinear fashion (maximal EPSP nonlinearity under control: $44 \pm 6\%$, $n = 11$ spines from 11 cells, peak difference of control versus 50–100 μM D-AP5 and 12.5 μM MK-801 for EPSP: $68 \pm 10\%$, $n = 11$ spines from 11 cells, and spine head $\Delta\text{F}/\text{F}$: $344 \pm 76\%$, $n = 8$ spines from 8 cells). These data were used to produce a multi-compartmental simulation that compared the level of cooperativity among synaptic inputs placed either onto spine compartments or directly onto dendrites (Fig. 4d–i). The simulations show that passive electrical amplification by spines promotes the recruitment of local active voltage-dependent conductances by multiple inputs, elevating the amount of above linear summation (Fig. 4e,f). Input cooperativity, quantified as the amount of supralinear depolarization provided by additional synaptic input, increases as a function of R_{neck} (Fig. 4g; Supplementary Fig. 8). In general, this augmentation of input cooperativity by spines (expressed as the fractional increase over the no-spine condition) initially increases then declines with additional inputs (Fig. 4h). The exact relationship of spine augmentation to input number is dependent on R_{neck} with a saturation effect beginning to occur for spines with $R_{\text{neck}} > 1.5 \text{ G}\Omega$ (dashed line; Fig. 4h). High impedance spines elevate peak cooperativity (up to $\sim 5\text{X}$) and mean cooperativity per input (up to $\sim 2\text{X}$) as a function of R_{neck} in both large apical trunk and small terminal branch dendritic compartments (Fig. 4i; see Supplementary Fig. 7 for model parameter ranges). The presence of high impedance spines therefore inherently augments input cooperativity by promoting electrical crosstalk between coactive synaptic inputs, providing a mechanism whereby activity-dependent changes in R_{neck} can regulate synaptic efficacy and nonlinear dendritic processing among potentiated synapses^{14,15}.

Our results provide insight into how the intrinsic properties of dendritic spines allow them to fundamentally shape neuronal processing and storage. Spines exhibit a high neck resistance (varying around 500 $\text{M}\Omega$) that passively amplifies local synaptic depolarization up to 50-fold. This amplification increases the activation of voltage-dependent processes within the spine head, enhances the interaction among coactive spines, and elevates nonlinear dendritic integration (Fig. 4, Supplementary Figs. 1 and 7). Furthermore, spines endow individual synapses with the ability to locally control the amount of passive (*i.e.* Ohmic) and active (*i.e.* voltage-dependent conductance-based) amplification they experience through the regulation of spine neck resistance^{5,14,15}. The amplifying and coordinating properties of dendritic spines we have described here will have a profound impact on neuronal input processing²⁶, and will also influence information storage by promoting the induction of clustered forms of synaptic and dendritic plasticity among coactive spines^{27–29}. Thus, spines enhance the ability of neurons to detect, uniquely respond to, and store distinct synaptic input patterns^{26,30}.

Methods

Hippocampal slice preparation

Acute, transverse hippocampal slices (400 μm) were prepared from 7 to 12 week-old male Sprague-Dawley and Wistar rats as described previously^{27,28}, according to methods approved by the Janelia Farm Institutional Animal Care and Use Committee and the Animal

Care and Use Committee (ACUC) of the Institute of Experimental Medicine, Hungarian Academy of Sciences, and was in accordance with 86/609/EEC/2 and DIRECTIVE 2010/63/EU Directives of the European Community. Briefly, animals were deeply anaesthetized with isoflurane and transcardially perfused with ice-cold cutting solution containing (in mM): sucrose 220, NaHCO₃ 28, KCl 2.5, NaH₂PO₄ 1.25, CaCl₂ 0.5, MgCl₂ 7, glucose 7, Na-pyruvate 3, and ascorbic acid 1, saturated with 95% O₂ and 5% CO₂. The brain was quickly removed and sectioned in cutting solution with a Vibratome (Leica). Slices were incubated in a submerged holding chamber in ACSF at 37°C for 30–60 min and then stored in the same chamber at room temperature. For recording, slices were transferred to the submerged recording chamber of the microscope where experiments were performed at 34–37°C in aCSF containing (in mM): NaCl 125, KCl 3, NaHCO₃ 25, NaH₂PO₄ 1.25, CaCl₂ 1.3, MgCl₂ 1, glucose 25, Na-pyruvate 3, and ascorbic acid 1, saturated with 95% O₂ and 5% CO₂. Except where described, NMDA receptors and voltage gated Na⁺ channels were blocked by continuous bath application of 50–100 μM D-AP5 (Tocris) and 0.5–1.0 μM tetrodotoxin (TTX, Tocris), respectively. In some experiments, 10–15 μM MK-801 (Tocris) was also present in the aCSF; no differences were observed, so data were combined. ZD7288, Nimodipine, MPEP, CPCOEt, NASPM (all from Tocris) and BaCl₂, NiCl₂, Cyclopiazonic acid (CPA), Philanthotoxin-433 (all from Sigma) were prepared as stock solutions, stored at –20°C and diluted directly to the extracellular solution on the day of the experiment.

Patch-clamp recording

Cells were visualized using an Olympus BX-61 epifluorescent microscope equipped with infrared Dodt optics and a water immersion lens (60X, 0.9 NA, Olympus, Melville, NY, USA). Current-clamp whole-cell recordings from the soma or apical dendrites of hippocampal CA1 pyramidal neurons were performed with Dagan BVC-700 amplifiers in the active ‘bridge’ mode, filtered at 3 kHz and digitized at 50 kHz. Patch pipettes (2–8 MΩ) were filled with a solution containing (in mM): K-Gluconate 134, KCl 6, HEPES 10, NaCl 4, Mg₂ATP 4, Tris₂GTP 0.3, Na-phosphocreatine 14, 0.05 Alexa 594 and 0.1 Oregon Green 488 BAPTA-1 (OGB-1, Invitrogen), pH 7.25. In some experiments (Supplementary Figs. 3 & 4), OGB-1 was replaced with 0.2 mM Fluo-4 or 0.2 mM Calcium Green-1 Dextran conjugate (70K MW, both from Invitrogen). Series resistance, monitored throughout the experiment, was <30 M Ω for perisomatic recordings and ranged from 12–40 M Ω for dendritic recordings. All neurons had resting membrane potentials between –62 and –68 mV (dendritic recordings) or –56 and –65 mV (somatic recordings) and were confirmed to have intact somas and tufts. For simulated EPSC injection during dual dendritic trunk recording (Fig. 1) we used a simple compartment model of a spine, spine neck and parent branch implemented in the Neuron modeling environment to determine the appropriate kinetics for current injection into the dendrite to mimic synaptic depolarization in the spine head. The resulting waveform is shown in Fig. 1c.

Two-photon imaging and uncaging

A dual galvanometer-based two-photon laser scanning system (Prairie Technologies, Middleton, WI, USA) was used to image neurons and to focally uncage glutamate at individual dendritic spines^{27,28}. Two ultrafast pulsed laser beams (Chameleon Ultra II;

Coherent, Auburn, CA, USA) were used: one at 880 and 920 nm for imaging Alexa 594 and OGB-1 (Molecular Probes, Eugene, OR, USA), respectively, and one at 720 nm to photolyze MNI-caged-L-glutamate (Tocris Cookson, Ballwin, MO, USA; 10 mM, dissolved in freshly carbogenated aCSF containing 50–100 μ M D-AP5 and 0.5–1.0 μ M tetrodotoxin unless otherwise noted and applied via pressure ejection through a pipette above the slice). Laser beam intensity was independently controlled with electro-optical modulators (Model 350–50, Conoptics, Danbury, CT, USA). Uncaging dwell time was 0.2 ms; galvo move time intervals varied depending on the experiment (see below). Linescan imaging through spines was performed at 150–500 Hz with dwell times of 8–12 μ s for <400 ms.

Particular care was taken to limit photodamage during imaging and uncaging. This included the use of a passive 8X pulse splitter in the uncaging path in most experiments to drastically reduce photodamage³¹. Basal fluorescence of both channels was continuously monitored as an immediate indicator of damage to cellular structures. Subtle signs of damage included decreases in or loss of phasic Ca^{2+} signals in spine heads in response to either uncaging or current injection, small but persistent depolarization following uncaging, and changes in the kinetics of voltage responses to uncaging or current injection. Experiments were terminated if neurons exhibited any of these phenomena.

Determination of AR and R_{neck}

Our experimental strategy was based on the biophysical property of asymmetric voltage attenuation across the spine neck due to the high impedance of the spine head relative to the low dendritic branch input impedance^{4,6,32}. Thus, EPSP-shaped voltage transients significantly attenuate only as they propagate out of the spine and into the dendrite. We exploited this feature to compute an amplitude ratio (AR) for EPSPs initiated in the spine and measured in the dendrite ($\text{EPSP}_{\text{branch}}$; so called because the measured EPSP amplitude reflects the spine potential after it has propagated across the spine neck into the branch) compared to those producing the same level of spine depolarization when initiated and measured in the dendrite ($\text{EPSP}_{\text{spine}}$; representing the EPSP amplitude in the spine head). Our computer model confirmed that AR magnitude is independent of the electrical recording site and that this method is sufficiently accurate to measure spine voltage AR throughout the CA1 dendritic arbor within stratum radiatum (Supplementary Fig. 8).

For the dual dendritic patch experiments shown in Fig. 1, the EPSPs evoked by uncaging at single spines exhibited an almost identical amplitude at both pipettes (1.41 ± 0.16 vs. 1.44 ± 0.15 mV, $n = 9$, $p = 0.3032$, paired t-test), demonstrating that the base of the dendrite at nearby spines is isopotential with the recording electrode. In addition, our morphologically realistic multi-compartmental model suggests that the trunk should be relatively isopotential to ~ 30 μ m proximal (towards the soma) and ~ 50 μ m distal from the electrode.

Calculation of spine neck resistance is based on the voltage divider equation (see Fig. 1h)⁸. EPSP amplitude at the spine head for a synapse on the spine is given by:

$$V_{\text{head}} = E_{\text{syn}} \frac{R_{\text{neck}} + R_{\text{dend}}}{1/G_{\text{syn}} + R_{\text{neck}} + R_{\text{dend}}} \quad (1)$$

where V_{head} is the EPSP amplitude in the spine head.

EPSP amplitude at the dendrite for a synapse on the spine is given by:

$$V_{dend} = E_{syn} \frac{R_{dend}}{1/G_{syn} + R_{neck} + R_{dend}} \quad (2)$$

where V_{dend} is the EPSP amplitude in the dendrite.

The ratio of the amplitudes (AR) is given by:

$$AR = \frac{R_{neck} + R_{dend}}{R_{dend}} = 1 + \frac{R_{neck}}{R_{dend}} \quad (3)$$

The resistance of the spine neck (R_{neck}) can be calculated from:

$$R_{neck} = (AR - 1) \times R_{dend} \quad (4)$$

Uncaging input paradigms

Because we cannot patch small diameter terminal branches, in order to measure spine-to-branch voltage amplitude ratio in these compartments, local dendritic current injection (as used in Fig. 1) was replaced with rapid multi-site glutamate uncaging onto neighboring spines near the spine of interest while recording the resultant EPSPs at the apical trunk (Fig. 2&3e, Supplemental Figs. 3,4,6c–f) or soma (Supplemental Figs. 2a–c and 6a&b). The speed at which each spine on a dendrite can be stimulated is limited by the uncaging galvanometers (in practice this is 0.3 ms per spine: 0.2 ms dwell time + 0.1 ms move time). Thus, to control for possible confounds in differential dendritic filtering along oblique branches, we matched the shape of depolarizations for EPSP_{branch} and EPSP_{spine} measured at the voltage recording electrode by using 15 (low-power) uncaging events at the single spine of interest versus 15 (higher power) uncaging events distributed at 15 neighboring spines on the same branch (Fig. 2, Supplementary Figs. 3,4). The branch uncaging input was performed at the galvanometer speed limit while the galvanometer move time was occasionally increased (up to 0.3 ms) for the 15 uncaging events at the single spine in order to match the kinetics of the two EPSPs. The computer model indicates that the kinetic slowing associated with this method decreased observed AR ~50% at dendritic trunk regions (Supplementary Fig. 8a; thus the AR values of ~22 for the trunk experiments conducted in this manner in Fig. 2e compared to the AR of ~45 measured by comparing a single uncaging event with fast current injection in Fig. 1) and ~15% at terminal branch locations (Supplementary Fig. 8b). However, at the distal tip of oblique branches, where the dendritic impedance is high due to the sealed end, we were able to conduct experiments comparing a single uncaging event at the spine of interest to uncaging at only 1–2 nearby neighbors (see Supplementary Fig. 5a–d) for the calculation of AR in this compartment (Fig. 2e, red symbols). Thus, we have accurate fast kinetic boundary conditions for AR at the trunk (using current injection, Fig. 1) and the distal dendritic tip (using 1–2 neighboring spines, Fig. 2e, red symbols) while the exact shape of the distribution of AR along the branch will

vary slightly depending on the frequency of the stimulation protocol. For some experiments measuring the relative effects of pharmacology on AR, we compared a single uncaging event at the spine of interest with uncaging at a number of neighboring spines (Fig. 3e, Supplementary Fig. 2b).

Data analysis

Analysis was performed using custom-written macros in IgorPro and MatLab. Ca^{2+} and voltage signals were analyzed offline using averaged traces of 3–10 trials with no smoothing or background subtraction. Some imaging trials exhibited a light artifact from the uncaging laser, which was excised. Ca^{2+} signal amplitude was measured as the maximum average of three consecutive points within 50 ms after uncaging. For calculation of AR, spine Ca^{2+} signals greater than 25% and less than 125% $\Delta\text{F}/\text{F}$ (the linear range of OGB-1; Invitrogen.com) were compared between stimulation paradigms at a range of different intensities. For branch vs. spine Ca^{2+} signals exhibiting less than 25% difference (average difference of $3.1 \pm 1.5\%$, $n = 109$ spines from 71 neurons, see also Supplementary Fig. 9) their respective EPSPs (larger than 1 mV for trunk spines recorded at the trunk $<50\ \mu\text{m}$ away, or larger than 0.5 mV for oblique spines recorded at the trunk or soma) were compared. All comparisons that fit these criteria for a given spine were averaged to compute AR for that paradigm at that spine.

Morphological and distance measurements were performed using ImageJ/FIJI (NIH) on two-dimensional maximal intensity projections of 1–2 μm z-series collected at the end of the experiment. Spines on apical oblique branches were categorized as proximal, middle or distal by division of the overall branch length into thirds.

Due to the necessity of clearly isolating a single spine for uncaging in order to accurately calculate AR (if multiple spines are activated by a single uncaging event, $\text{EPSP}_{\text{branch}}$ becomes artifactually large compared to the observed spine head Ca^{2+} signal and distorts AR), spines chosen for imaging were clearly separated from their parent dendrite (and nearby neighbors). Individual spines were selected to reflect the average phenotype of their neighbors along a branch, and did not exhibit overly large heads or long necks, presumably falling into an intermediate category between or spanning the previously described “stubby” and “mushroom” types. At the beginning of an experiment, Ca^{2+} signals in response to single spine uncaging at various laser powers were first measured and only those spines where the Ca^{2+} signal and EPSP amplitude increased incrementally as a function of power were further studied. This criterion was met in most spines of the apical trunk and oblique dendrites. However in a subgroup of spines, primarily on oblique branches, Ca^{2+} signals were either small and unreliable or did not increase proportional to increasing stimulation. These recordings were not included in this study. For the long spine neck experiments in Supplementary Fig. 6a–b, we searched the dendritic arbor for the longest necked spines we could find (which appeared to constitute $<1\%$ of the overall spine population) to measure AR.

Computational methods

All simulations were performed using the NEURON simulation environment³³ with the variable time step (CVODE) method. The CA1 pyramidal neuron morphology used in the simulations was reconstructed from a rat hippocampal pyramidal neuron described previously^{34,35}. The model included a membrane capacitance of 1 $\mu\text{F}/\text{cm}^2$ and an axial resistivity of 150 $\Omega\text{-cm}$. The membrane resistivity was taken to be 20000 $\Omega\text{-cm}^2$ at the soma and to drop linearly as a function of distance to 2500 $\Omega\text{-cm}^2$ at a distance of 100 μm and beyond to reflect, in a simple way, the observed greater density of voltage-gated channels observed experimentally in these cells^{36,37}. As a result, the somatic input resistance was observed to be 27 M Ω , and the input resistance 200 μm from the soma along the main apical dendrite was 23 M Ω .

A second model (uniform R_D model) was constructed to produce a relatively constant local dendritic input impedance along apical oblique branches while maintaining the measured amount of amplitude filtering down the branches. This required reductions in both axial and membrane resistivity coordinated with dendritic diameter, implemented via gradients of axial (from 28 to 150 $\Omega\text{-cm}$; branch tip to trunk) and membrane resistivities (from 28 to 2500 $\Omega\text{-cm}^2$; branch tip to trunk) in a specific oblique dendrite (branching from the main apical dendrite approximately 300 μm from the soma) according to the following formulae:

$$r_L(x) = r_L(0) [a(x)/a(0)]^\alpha$$

and

$$r_m(x) = r_m(0) [a(x)/a(0)]^\beta$$

where x is the distance along the oblique branch measured from the main apical dendrite, r_L is axial resistivity, r_m is membrane resistivity, a is dendrite diameter, and $\alpha = 1.5$, $\beta = 4$. The selected branch had an approximately constant input impedance over most of its length (~50–60 M Ω over ~200 μm). This model could reproduce the observed dependence of amplitude ratio upon distance along the oblique dendrite if the spine neck resistance was also dependent upon distance. A prediction for the required spine neck resistance (R_N) can be computed from

$$R_N = (AR - 1)R_D$$

where AR is the desired target amplitude ratio and R_D is the dendritic input impedance. Spine neck resistance for this condition ranged from 39.7 to 465.1 M Ω from tip to trunk. A variable increase in synaptic conductance approaching 10-fold (20 to 2.0 nS from tip to trunk) was also required to match data shown in Fig. 2d. However, in the uniform R_D model several key fundamental electrophysiological properties move far out of reported experimental ranges. First, the membrane time constant becomes very small (<100 μs) because of the large leak conductance. Reported experimental measures are two orders of

magnitude larger^{32,36}. Second, the impedance load of each dendrite branch increases significantly causing enhanced attenuation of signals propagating from dendrite to soma. In the standard model the maximum amount of attenuation from the distal apical trunk to the soma was 6.4 while in the uniform R_D model the level of attenuation was 46.9. Finally, the manipulations caused the input resistance at the soma to drop to 6 $M\Omega$. These values are both approximately an order of magnitude out of the range of what has been observed experimentally^{32,36}. Altogether, the need for coordinated 5–10X manipulations of axial resistivity, membrane resistivity, spine neck resistance and synaptic conductance contradicts experimental evidence³⁸ and is extremely implausible.

In both models, spines were modeled as a cylindrical compartment representing the spine neck with length 1.58 μm and diameter 0.077 μm and a spherical head with diameter 0.5 μm ; with an axial resistivity of 150 $\Omega\text{-cm}$, this produced a spine neck resistance of 500 $M\Omega$. Simulations of spines placed directly on the dendrite were modeled by reducing the neck length to 0.01 μm and increasing the diameter to 0.5 μm (to match the spine head diameter). AMPA synapses were modeled as a double-exponential conductance function with rise time 0.1 ms, decay time 1 ms and reversal potential 0 mV. For simulations involving only AMPA synapses, the peak conductance was adjusted dynamically at each location in the dendritic tree using a root-finding algorithm³² to reach a target depolarization in the spine head of 35 mV; results were not strongly dependent upon the specific target voltage used. Modeling of low-power multi-event or rapid multi-site glutamate uncaging was performed computationally by activating a series of synapses with a 0.3 ms delay between events. To speed up simulations of single-site multiple events, the series of double-exponential AMPA conductances was replaced with a single, averaged conductance. To do the averaging, one starts with a double-exponential synapse that turns on at the source time s ,

$$g = g_{\max} C (e^{-(t-s)/\tau_2} - e^{-(t-s)/\tau_1}) \quad \text{for } t > s.$$

The constant C is chosen so that the maximum of the right-hand-side is g_{\max} . Note that here we are assuming that $\tau_1 < \tau_2$; τ_1 is the rise time, and τ_2 is the decay time. If we now suppose that synapses are distributed over the time interval $0 < s < T$ with conductance $g_{\max} = g(s)ds$, and we add up these individual contributions,

$$g = \int_0^{\min(t,T)} g(s) C (e^{-(t-s)/\tau_2} - e^{-(t-s)/\tau_1}) ds.$$

Note the upper limit $\min(t,T)$ is due to causality; for $t < T$ one only has contributions for $0 < s < t$; when $t > T$, however, one gets contributions for the whole range, $0 < s < T$. If one assumes a uniform distribution of synaptic strength over time (*i.e.* each successive uncaging event elicits exactly the same amount of synaptic response), one can take $g(s) = 1$ and evaluate the integral. The result is

$$g/C = \tau_2(1 - e^{-t/\tau_2}) - \tau_1(1 - e^{-t/\tau_1}) \quad \text{for } t < T,$$

$$g/C = \tau_2(1 - e^{-T/\tau_2})e^{-(t-T)/\tau_2} - \tau_1(1 - e^{-T/\tau_1})e^{-(t-T)/\tau_1} \quad \text{for } t > T.$$

The maximum of this function can be determined and C chosen to normalize the conductance. Because it was found that computational models of rapid multi-site glutamate uncaging depended very weakly upon spine location, as long as spines were within a spatial range of a few tens of μm of one another, the above averaged conductance was also used to simulate multi-site glutamate uncaging. The amplitude ratio can depend strongly on the additional time interval over which synaptic current is distributed. Supplementary Fig. 8 shows the result of simulations for a synapse on a spine located either on the main apical trunk approximately 200 μm from the soma, or on an apical oblique dendrite roughly 80% of the distance along the oblique from the trunk to the tip of the oblique. For the case of the spine on the apical trunk, as the time interval T increases from 0 to 6 ms, the amplitude ratio decreases from more than 40 to approximately 20. Further increases in the time interval cause relatively small further decreases in the AR, as the value asymptotes to the amplitude ratio for steady-state currents. For the case of the spine on the oblique, the amplitude ratio is largely independent of the spread time of the synaptic current. In simulations including NMDA synapses, the AMPA conductance was set at 0.7–1 nS. NMDA synapses were modeled as a double-exponential conductance function with rise time 1 ms, decay time 75 ms, peak 1.4–3.0 nS and reversal potential 0 mV. In addition, for NMDA synapses a voltage-dependent factor

$$g(V) = \frac{1}{1 + \exp(-0.062V[mg]/3.57)}$$

multiplied the total conductance, where V is the membrane potential in mV, and $[mg]$ is the extracellular magnesium concentration in mM, to model the relief of the voltage-dependent magnesium block of NMDA channels. A magnesium concentration of 1 mM was used in all simulations.

Supplementary Material

Refer to Web version on PubMed Central for supplementary material.

Acknowledgments

We thank A. Milstein, S. Gale and R. Chitwood for help in creating analysis tools, and G. Murphy, S. Williams, and D. Johnston for constructive criticism. This work was supported by the Howard Hughes Medical Foundation, NIH (NS-046064), and a Wellcome Trust International Senior Research Fellowship to J.K.M. (090915/Z/09/Z).

References

1. Ramón y Cajal S. Estructura de los centros nerviosos de las aves. *Rev Trim Histol Norm Patol.* 1888; 1:1–10.
2. Bourne JN, Harris KM. Balancing structure and function at hippocampal dendritic spines. *Annu Rev Neurosci.* 2008; 31:47–67. [PubMed: 18284372]

3. Rall W. Theory of physiological properties of dendrites. *Ann N Y Acad Sci.* 1962; 96:1071–1092. [PubMed: 14490041]
4. Rall, W. Dendritic spines, synaptic potency and neuronal plasticity. In: Woody, CD., et al., editors. *Cellular Mechanisms Subserving Changes in Neuronal Activity.* Brain Information Research Report #3. Los Angeles: University of California; 1974.
5. Miller JP, Rall W, Rinzel J. Synaptic amplification by active membrane in dendritic spines. *Brain Res.* 1985; 325:325–330. [PubMed: 2983830]
6. Koch C, Zador A. The function of dendritic spines: devices subserving biochemical rather than electrical compartmentalization. *J Neurosci.* 1993; 13:413–422. [PubMed: 8426220]
7. Yuste R. Dendritic spines and distributed circuits. *Neuron.* 2011; 71:772–781. [PubMed: 21903072]
8. Hao J, Oertner TG. Depolarization gates spine calcium transients and spike-timing-dependent potentiation. *Curr Opin Neurobiol.* Nov 1.2011 [Epub ahead of print].
9. Guthrie PB, Segal M, Kater SB. Independent regulation of calcium revealed by imaging dendritic spines. *Nature.* 1991; 354:76–80. [PubMed: 1944573]
10. Yuste R, Denk W. Dendritic spines as basic functional units of neuronal integration. *Nature.* 1995; 375:682–684. [PubMed: 7791901]
11. Yasuda R, Murakoshi H. The mechanisms underlying the spatial spreading of signaling activity. *Curr Opin Neurobiol.* 2011; 21:313–21. [PubMed: 21429735]
12. Chen Y, Sabatini BL. Signaling in dendritic spines and spine microdomains. *Curr Opin Neurobiol.* Mar 26.2012 [Epub ahead of print].
13. Svoboda K, Tank DW, Denk W. Direct measurement of coupling between dendritic spines and shaft. *Science.* 1996; 272:716–719. [PubMed: 8614831]
14. Grunditz A, Holbro N, Tian L, Zuo Y, Oertner TG. Spine neck plasticity controls postsynaptic calcium signals through electrical compartmentalization. *J Neurosci.* 2008; 28:13457–13466. [PubMed: 19074019]
15. Bloodgood BL, Sabatini BL. Neuronal activity regulates diffusion across the neck of dendritic spines. *Science.* 2005; 310:866–869. [PubMed: 16272125]
16. Palmer LM, Stuart GJ. Membrane potential changes in dendritic spines during action potentials and synaptic input. *J Neurosci.* 2009; 29:6897–6903. [PubMed: 19474316]
17. Bloodgood BL, Giessel AJ, Sabatini BL. Biphasic synaptic Ca influx arising from compartmentalized electrical signals in dendritic spines. *PLoS Biol.* 2009; 7:e1000190. [PubMed: 19753104]
18. Tsay D, Yuste R. On the electrical function of dendritic spines. *Trends Neurosci.* 2004; 27:77–83. [PubMed: 15102486]
19. London M, Häusser M. Dendritic computation. *Annu Rev Neurosci.* 2005; 28:503–32. [PubMed: 16033324]
20. Wu XE, Mel BW. Capacity-enhancing synaptic learning rules in a medial temporal lobe online learning model. *Neuron.* 2009; 62:31–41. [PubMed: 19376065]
21. Legenstein R, Maass W. Branch-specific plasticity enables self-organization of nonlinear computation in single neurons. *J Neurosci.* 2011; 31:10787–802. [PubMed: 21795531]
22. Magee JC, Cook EP. Somatic EPSP amplitude is independent of synapse location in hippocampal pyramidal neurons. *Nat Neurosci.* 2000; 3:895–903. [PubMed: 10966620]
23. Bloodgood BL, Sabatini BL. Nonlinear regulation of unitary synaptic signals by CaV(2.3) voltage-sensitive calcium channels located in dendritic spines. *Neuron.* 2007; 53:249–260. [PubMed: 17224406]
24. Jaffe DB, Carnevale NT. Passive normalization of synaptic integration influenced by dendritic architecture. *J Neurophysiol.* 1999; 82:3268–85. [PubMed: 10601459]
25. Gullledge AT, Carnevale NT, Stuart GJ. Electrical advantages of dendritic spines. *PLoS One.* 2012; 7:e36007. [PubMed: 22532875]
26. Branco T, Clark BA, Häusser M. Dendritic discrimination of temporal input sequences in cortical neurons. *Science.* 2010; 329:1671–1675. [PubMed: 20705816]
27. Losonczy A, Makara JK, Magee JC. Compartmentalized dendritic plasticity and input feature storage in neurons. *Nature.* 2008; 452:436–441. [PubMed: 18368112]

28. Makara JK, Losonczy A, Wen Q, Magee JC. Experience-dependent compartmentalized dendritic plasticity in rat hippocampal CA1 pyramidal neurons. *Nat Neurosci.* 2009; 12:1485–1487. [PubMed: 19898470]
29. Harvey CD, Svoboda K. Locally dynamic synaptic learning rules in pyramidal neuron dendrites. *Nature.* 2007; 450:1195–1200. [PubMed: 18097401]
30. Gasparini S, Magee JC. State-dependent dendritic computation in hippocampal CA1 pyramidal neurons. *J Neurosci.* 2006; 26:2088–2100. [PubMed: 16481442]
31. Ji N, Magee JC, Betzig E. High-speed, low-photodamage nonlinear imaging using passive pulse splitters. *Nature Methods.* 2008; 5:197–202. [PubMed: 18204458]
32. Johnston, D.; Wu, S. *Foundations of Cellular Neurophysiology.* MIT Press; Cambridge MA: 1995. p. 400-411.
33. Hines ML, Carnevale NT. The neuron simulation environment. *Neural Computation.* 1997; 9:1179–1209. [PubMed: 9248061]
34. Golding NL, Kath WL, Spruston N. Dichotomy of action-potential backpropagation in CA1 pyramidal neuron dendrites. *J Neurophysiol.* 2001; 86:2998–3010. [PubMed: 11731556]
35. Golding NL, Mickus TJ, Katz Y, Kath WL, Spruston N. Factors mediating powerful voltage attenuation along CA1 pyramidal neuron dendrites. *J Physiol.* 2005; 568:69–82. [PubMed: 16002454]
36. Magee JC. Dendritic Ih normalizes temporal summation in hippocampal CA1 neurons. *Nat Neurosci.* 1999; 2:508–514. [PubMed: 10448214]
37. Hoffman DA, Magee JC, Colbert CM, Johnston D. K⁺ channel regulation of signal propagation in dendrites of hippocampal pyramidal neurons. *Nature.* 1997; 387:869–875. [PubMed: 9202119]
38. Katz Y, Menon V, Nicholson DA, Geinisman Y, Kath WL, Spruston N. Synapse distribution suggests a two-stage model of dendritic integration in CA1 pyramidal neurons. *Neuron.* 2009; 63:171–7. [PubMed: 19640476]

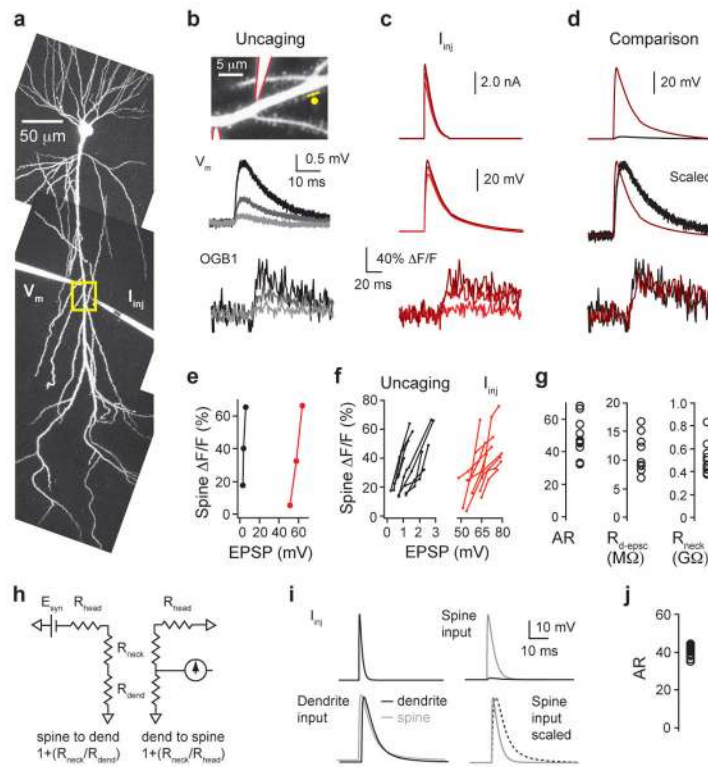


Figure 1. Measurement of voltage amplitude ratio across apical trunk spine necks

a, Two-photon z-stack of a CA1 pyramidal neuron patched with two electrodes at the apical trunk $\sim 200 \mu\text{m}$ from the soma. **b**, Top: yellow box from (a) expanded to show spine imaging (yellow line) and two-photon glutamate uncaging (yellow dot) locations. Electrodes are outlined in red. Averaged voltage traces (middle) and spine Ca^{2+} signals (bottom) evoked by uncaging at increasing laser powers. **c**, EPSC-shaped waveforms delivered through one electrode (top) evoked EPSPs recorded at the other electrode (middle) and spine Ca^{2+} signals (bottom). **d**, Comparison of voltage traces (top: actual amplitude, middle: scaled) corresponding to similar spine Ca^{2+} signals (bottom). **e**, Spine Ca^{2+} signals versus EPSP amplitude evoked by single spine glutamate uncaging (black) and EPSC injection (red) for the cell in (a–d). **f**, Summary of 10 experiments comparing single trunk spine uncaging with current injection during dual dendritic recording. **g**, Amplitude ratio ($\text{AR})_{2+}$ calculated from $\text{EPSP}_{\text{spine}}/\text{EPSP}_{\text{branch}}$ at comparable spine Ca signals (left) for experiments shown in (f) and associated peak dendritic input resistance during EPSC injection ($R_{\text{d-epsc}}$; middle) were used to derive spine neck resistance (R_{neck} ; right). **h**, Circuit diagram for voltage attenuation from dendrite to spine versus spine to dendrite across spine head, spine neck, and dendritic resistances. **i**, Voltage responses at the dendrite (black) or spine head (gray) in a multi-compartment model of a CA1 neuron for a trunk spine $213 \mu\text{m}$ from the soma with a $500 \text{ M}\Omega$ neck resistance in response to fast current injection at either the spine head or dendrite. **j**, Summary of $\text{EPSP}_{\text{spine}}/\text{EPSP}_{\text{branch}}$ amplitude ratio for 18 model trunk spines located $150\text{--}300 \mu\text{m}$ from the soma.

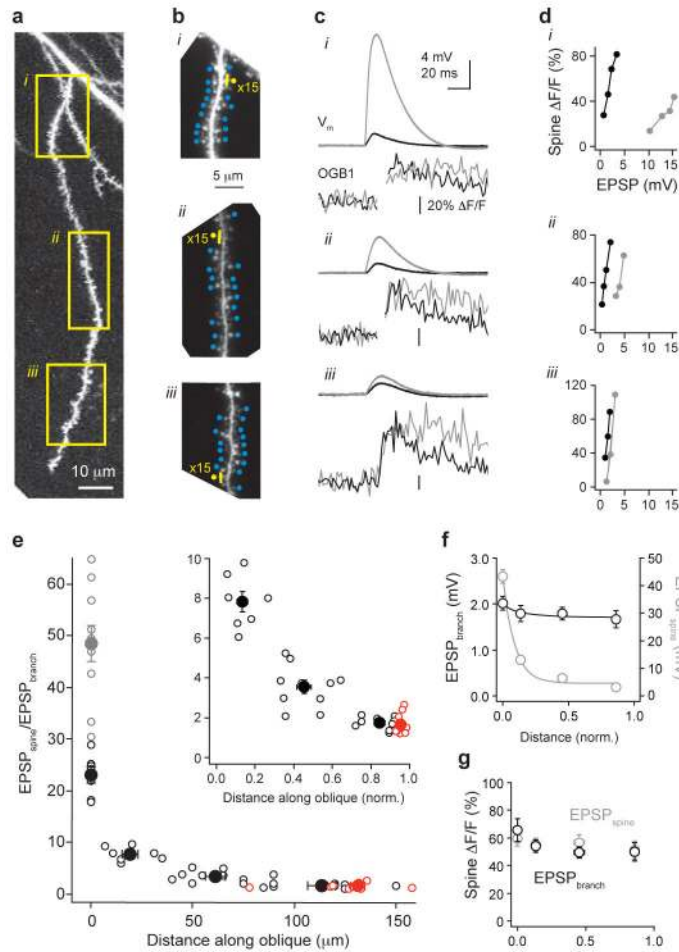


Figure 2. Spine neck voltage amplitude ratio varies as a function of dendritic compartment
a, Z-stack image showing uncaging locations (yellow boxes) along a single apical oblique dendrite which branches from the trunk 250 μm from the soma. **b**, Increased magnification of the areas indicated in (a) showing locations for imaging (yellow line) and uncaging (yellow circles) at the spine of interest or at 15 nearby spines (blue circles). **c**, Voltage traces (recorded in the apical trunk, upper) corresponding to comparable spine Ca^{2+} signals (lower) evoked by stimulation of the spine of interest with 15 low-power uncaging pulses (black) or 15 neighboring spines (gray) at the three input sites indicated in (a & b). Note the similar EPSP kinetics for the two stimulation paradigms. **d**, Relationship between EPSP amplitude and spine head Ca^{2+} signals for single spine (black) versus neighboring spines (gray) stimulation along the oblique branch. **e**, Spine-to-branch voltage AR as a function of dendritic compartment. Black: experiments conducted using uncaging at 15 neighboring spines for $\text{EPSP}_{\text{spine}}$ (as per a–d), red: experiments conducted at distal tips of oblique dendrites using single stimulation of the spine of interest compared with only 1–2 neighboring spines, gray: single uncaging at trunk spines versus EPSC injection during dual dendritic recording (from Fig. 1; see Methods for discussion of different AR measurement paradigms). Inset shows AR along oblique branches as a function of normalized branch length. **f**, Amplitudes of $\text{EPSP}_{\text{branch}}$ (black) and $\text{EPSP}_{\text{spine}}$ (grey) used to calculate AR as a function of normalized distance along apical oblique dendrites for experiments conducted as

described in (a–d), from black data points in (e). **g**, Corresponding spine head Ca^{2+} signals for EPSP_{branch} (black) and EPSP_{spine} (grey) from (f). Error bars show s.e.m.

Author Manuscript

Author Manuscript

Author Manuscript

Author Manuscript

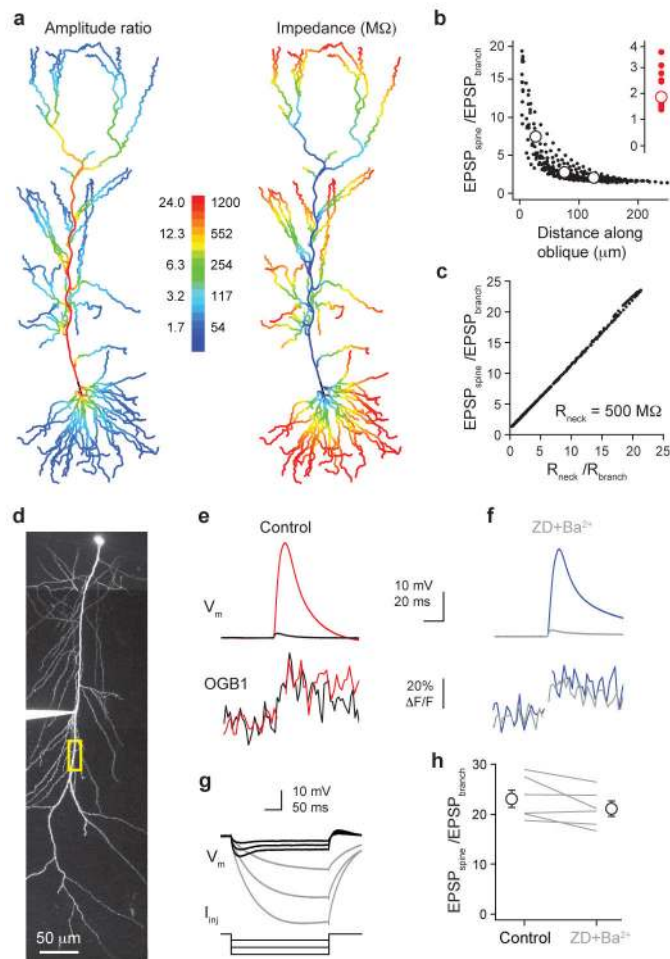


Figure 3. Spine-to-branch voltage compartmentalization is mediated by dendritic impedance
a, Left, spatial distribution of AR for spines with $500 \text{ M}\Omega$ R_{neck} in the model CA1 neuron (stimulation conducted as described for Fig. 2a–d). Right, local impedance across all compartments in the model. **b**, Modeling results for 323 spines (black) located on apical oblique branches that originated from the trunk $150\text{--}400 \mu\text{m}$ from the soma. Open circles represent bins of the first, second and third $50 \mu\text{m}$ along the obliques. Error bars are within the symbols. Inset shows AR for 26 model spines located within $8 \mu\text{m}$ of the tip of an oblique as per (Fig. 2e), red. **c**, The degree of voltage attenuation across spine necks in the model closely matches the ratio of R_{neck} to R_{branch} . **d**, Image stack of a CA1 pyramidal cell patched $215 \mu\text{m}$ from the soma. Yellow box indicates region of interest for trunk spine imaging and uncaging. **e**, Example voltage traces (top) of $\text{EPSP}_{\text{spine}}$ (red; evoked by uncaging at 30 neighboring trunk spines) and $\text{EPSP}_{\text{branch}}$ (black; evoked by single uncaging at spine of interest) for comparable spine Ca^{2+} signals (bottom) under control conditions. **f**, Example voltage traces of $\text{EPSP}_{\text{spine}}$ (blue) and $\text{EPSP}_{\text{branch}}$ (grey) for comparable spine Ca^{2+} signals after application of $10 \mu\text{M}$ ZD7288 and $400 \mu\text{M}$ Ba^{2+} for the same spine in (e). **g**, Effect of ZD7288 and Ba^{2+} on dendritic voltage responses evoked by $100\text{--}300 \text{ pA}$ hyperpolarizing step current injections at -65 mV for the cell in (d–f) (control: black, ZD

+Ba²⁺: grey). **h**, Summary of the effect of ZD and Ba²⁺ on spine-to-trunk amplitude ratio for 6 spines from 6 dendritic recordings. Error bars show s.e.m.

Author Manuscript

Author Manuscript

Author Manuscript

Author Manuscript

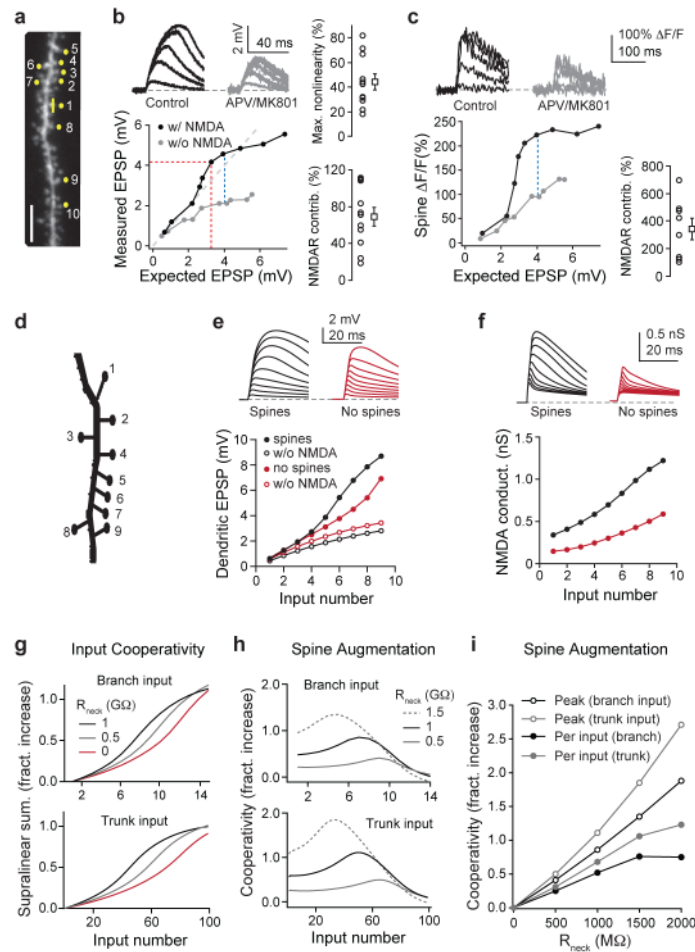


Figure 4. Spines enhance the cooperative interaction among multiple inputs

a, Oblique dendrite with trunk branch point 150 μm from the soma illustrating linescan profile (yellow line) and uncaging locations (yellow dots with numbers showing sequence). Scale bar: 5 μm . **b**, Example voltage traces (top; every second trace shown) and expected vs. measured EPSP plot (bottom) for uncaging at increasing numbers of spines under control conditions (black) and in the presence of NMDAR antagonists (grey), recorded at trunk. Grey dashed line indicates unity. Colored dashed lines indicate measurements of maximal nonlinearity (red, population data shown at top right, $n = 11$) and contribution of NMDAR to the input-output relationship (blue, population data shown at bottom right, $n = 11$). **c**, Example fluorescence traces (top; every second trace shown) and plot vs. expected EPSP from spine 1 during recruitment of increasing numbers of neighboring spines under control conditions (black) and in the presence of NMDAR antagonists (grey). Blue dashed line indicates measurement of NMDAR contribution to spine head Ca^{2+} signals (population data shown at bottom right, $n = 8$). **d**, Schematic of model conditions in an oblique branch. **e**, Dendritic trunk voltage traces (top) and dendritic trunk input-output voltage relationship (bottom) with synapses onto spines (black) and onto collapsed spines (red) for the model oblique branch shown in (d). Similar curves are shown without NMDAR present (open red or black). **f**, Spine NMDAR conductance traces (top) and spine NMDAR activation vs. input

number (bottom) with synapses onto spines (black) and onto collapsed spines (red) for the oblique branch shown in (d). **g**, The greater than linear component of input-output curves expressed as the fractional increase over linear summation for inputs ($G_{\text{AMPA}} = 0.7 \text{ nS}$; $G_{\text{NMDAR}} = 1.4 \text{ nS}$) onto a terminal oblique branch or apical trunk near the branch. Input number was increased until the peak of supra-linear summation was approached. **h**, Augmentation of input cooperativity by spines expressed as fractional increase in cooperativity over level achieved by no-spine input (fractional difference of $R_{\text{neck}} > 0$ and $R_{\text{neck}} = 0$ summation curves as in g). **i**, Spine augmentation of peak and mean input cooperativity expressed as a function of R_{neck} . Peak and mean cooperativity values are taken from plots in (h).